Journal of Sea Research 107 (2016) 12–24

Contents lists available at ScienceDirect

Journal of Sea Research

journal homepage: www.elsevier.com/locate/seares

A coupled physical–biological modeling study of the offshore phytoplankton bloom in the Taiwan Strait in winter

Jia Wang *, Huasheng Hong, Yuwu Jiang

State Key Laboratory of Marine Environmental Science, Xiamen University, Xiamen 361005, Fujian, PR China

ARTICLE INFO

Article history:
Received 2 March 2015
Received in revised form 5 November 2015
Accepted 11 November 2015
Available online 14 November 2015

Keywords:
Winter bloom
Cross-strait flow
Stratification
Critical turbulence intensity
Asian monsoon
Wind relaxation

ABSTRACT

In-situ observations find that offshore phytoplankton blooms occur occasionally in the north-central Taiwan Strait (TWS) in winter, but the formation mechanisms behind are not yet understood. We simulate the offshore bloom scenario in the winter of 1998 with a coupled physical–biological numerical model. Model results illustrate that when the northeasterly wind is relaxed, a cross-strait current is induced, which carries diluted Min-Zhe Coastal Water (MZCW) offshore, extending into the upper layer of the western TWS. Vertical mixing is weakened in the western TWS due to intensified stratification formed by the location of fresh MZCW over saline water. Consequently, the vertical diffusion of chlorophyll decreases, and the bloom occurs in the upper layer of the western TWS. Additionally, the cross-strait current carries the high chlorophyll concentration from near-shore to offshore regions, forming a maximal offshore chlorophyll concentration. We propose that the relaxation of the northeasterly wind acts as a trigger for the winter bloom occurrence in the TWS through complicated physical processes, i.e., the diluted MZCW extending offshore, the stratification intensifying and mixing weakening, forming distinctive characteristics of winter blooms in the TWS.

1. Introduction

The Taiwan Strait (TWS) connects the East China Sea and South China Sea and is located in the western Pacific (Fig. 1). The circulation structure of the TWS is controlled strongly by the Asian monsoon (Hu et al., 2010). A strong northeasterly wind prevails in the region during winter (December to February), with a mean speed of approximately 10.2 m s^{-1} (Hu et al., 2010); the corresponding general circulation structure is shown in Fig. 1. The strong wind drives the cold, fresh and nutrient-rich Min-Zhe Coastal Water (MZCW), which flows into the strait along the Chinese coast. Meanwhile, the South Mixing Water (SMW), which is composed of warmer and higher salinity Kuroshio branch water and South China Sea subsurface water, intrudes into the strait from the southeastern canyon, i.e., the Penghu Channel (Hu et al., 2010; Jan et al., 2002; Wang and Chern, 1988).

The MZCW provides sufficient nutrients for phytoplankton growth in the TWS. However, the phytoplankton biomass in the TWS is relatively low in winter, with a mean chlorophyll concentration of less than 1.0 mg m^{-3} (Zhang, 2001; Zhang and Huang, 2000). Winter mean chlorophyll data detected of the Moderate Resolution Imaging Spectroradiometer (MODIS) (Fig. 2) over 10 years (2002–2012) indicate that the surface chlorophyll concentration is approximately 1.0–2.0 mg m^{-3} in the central TWS. However, anomalously high chlorophyll concentrations (approximately 2.5–3.0 mg m^{-3}) compared to the climatological winter status were found in the north-central TWS from the transect observations in the winters of 1998 (Zhang and Huang, 2000; Naik and Chen, 2008) (indicated by the red shadows in Fig. 2). These anomalously high chlorophyll concentrations are labeled as the winter offshore bloom in the TWS.

Mixing is typically intensive in the TWS during winter due to strong wind speeds. The occurrence of the offshore bloom is beyond our understanding under such kinetic conditions. Because of the severe sea state in winter, there are limited cruise data to explain the existence of the offshore bloom. Furthermore, the satellite chlorophyll data are scarce due to large cloud cover. Hence, the mechanisms driving bloom occurrence are not yet understood.

We use a coupled physical–biological model to study a winter offshore bloom scenario in 1998. The model description and evaluation are given in Section 2. In Section 3, the modeled biological and physical results illustrate a weakened mixing effect on bloom production due to a relaxation of the northeasterly wind. In Section 4, an analytical model further confirms the mixing effect on bloom production. Subsequently, we emphasize that an intensified stratification plays a dominant role in reducing mixing. Moreover, the effect of advection on maximal offshore chlorophyll formation is discussed. Finally, the physical and biological processes that induce bloom are summarized in Section 5.

* Corresponding author.
E-mail address: wangjia_123@xmu.edu.cn (J. Wang).

http://dx.doi.org/10.1016/j.seares.2015.11.004
1385-1101/

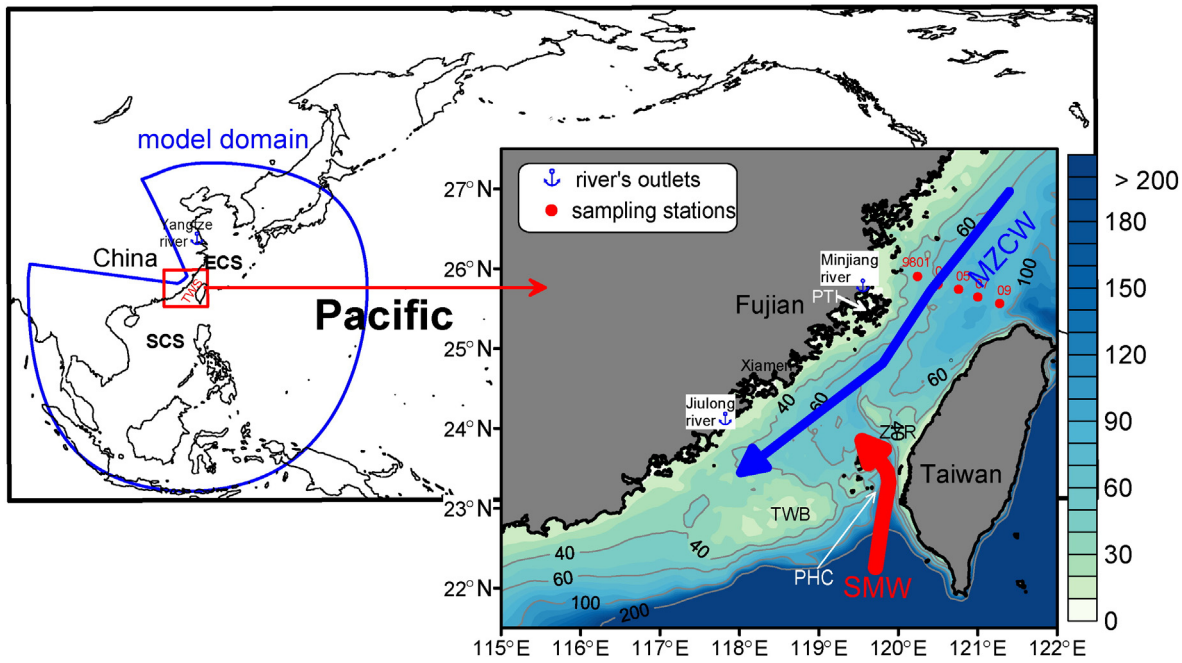

Fig. 1. Model domain and bathymetry (with isobaths shown) of the Taiwan Strait, which is indicated by the red box (inset). The red dots mark the cruise sampling stations (9801–9809) in 1998. The blue anchor symbol indicates river's outlet. The thick arrowed lines indicate the main circulation in the strait in winter: MZCW for the Min-Zhe Coastal Water (blue), SMW for South Mixing Water (red), ECS: East China Sea, SCS: South China Sea, TWS: Taiwan Strait, PTI for Pingtan Island, PHC for the Penghu Channel, ZYR for Zhangyun Ridge, and TWB for the Taiwan Bank. (For interpretation of the references to color in this figure legend, the reader is referred to the web version of this article.)

2. Model description and evaluation

2.1. Physical model

The physical model used in this study is the Regional Ocean Model System (Shchepetkin and McWilliams, 2005), which is a primitive equation model under hydrostatic and Boussinesq assumptions. The model has a curvilinear-orthogonal grid in the horizontal direction, and the grid size varies from 40 km at the open boundary to 1.5 km in the TWS. The model domain covers the northwestern Pacific from 93.13°E to 147.68°E and from 8.54°S to 44.9°N (see the inset in Fig. 1).

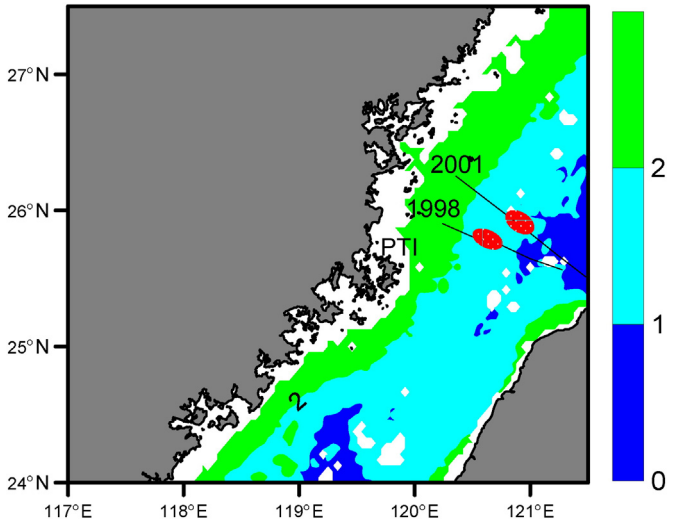

Fig. 2. Climatological mean chlorophyll in winter (December–February) (unit: mg m^{-3}) derived from MODIS 1992–2012 daily data. The red shadows indicate the anomalous offshore blooms (2–3 mg m^{-3}) observed in 1998 and 2001, respectively. The black lines show the observation sections. (For interpretation of the references to color in this figure legend, the reader is referred to the web version of this article.)

The water column is vertically divided into 30 layers following the S-coordinate scheme (Song and Haidvogel, 1994), with an enhanced resolution in the euphotic zone. The average depth is approximately 60 m in the TWS, and the vertical resolution ranges from 0.1 to 5 m from surface to bottom. The vertical mixing coefficient is calculated using the Mellor and Yamada 2.5-turbulence closure model (Mellor, 2001; Mellor and Yamada, 1982). The model bathymetry is interpolated from 2-minute global relief data and combined with the digitized depth data along the Chinese coast published by China's Maritime Safety Administration.

2.2. Biological model

A nitrogen-based nutrient–phytoplankton–zooplankton–detritus model (Fennel et al., 2006) is coupled with the physical model. The model schematic is shown in Fig. 3. Separating new and regenerative productivity processes and considering the aggregate effect of detritus, the model contains seven state variables: nitrate (NO_3), ammonium (NH_4), phytoplankton (PHYTO), chlorophyll (CHLO), zooplankton (ZOOP), small detritus (SDET), and large detritus (LDET). The relationship between chlorophyll and phytoplankton biomass is calculated using the method of Geider et al. (1996, 1997), which considers the change in chlorophyll content per phytoplankton cell relative to changes in light and nutrient conditions. NO_3 and NH_4 support new and regenerated productivities, respectively. The model also considers the inhibition of NO_3 uptake by NH_4. The detritus is divided into large and small components according to size. The mortality of phytoplankton and inefficient ingestion by zooplankton generate small detritus. Small detritus can aggregate with the phytoplankton to form large detritus in the model. A fraction of the detritus is mineralized into NH_4 in the water column, with the remaining fraction sinking toward the seabed.

In this study, we adopt the simplified scheme of coupling pelagic and benthic systems, as proposed by Soetaert et al. (2000), where the organic matter that reaches the bottom of the domain is immediately re-mineralized into NH_4 and added to the water composition in this region. The advantage of this scheme is that it ensures mass conservation in both

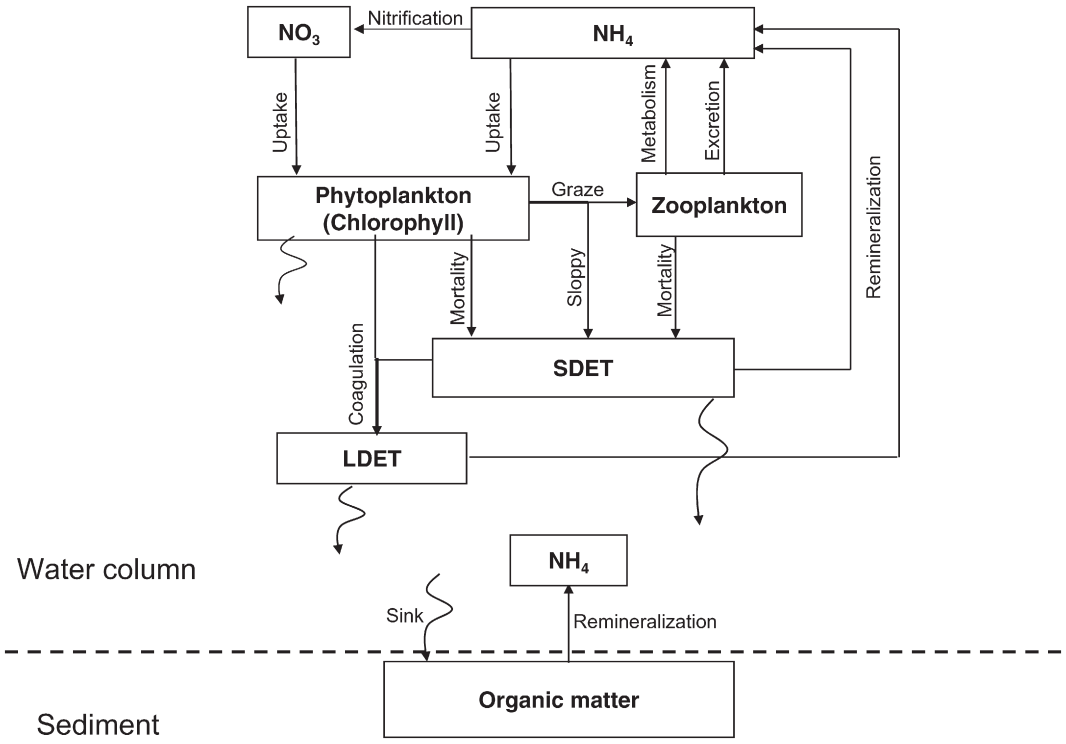

Fig. 3. Schematic for the biological model. SDET: small detritus; and LDET: large detritus.

systems, while capturing the essential dynamics of the pelagic–benthic coupling.

Because the main primary biological processes in the model are classic formulas, such as the temperature-dependent growth rate of phytoplankton (Eppley, 1972), the photosynthesis–light curve relationship (Evans and Parslow, 1985), and the Holling-type zooplankton grazing rate, a majority of the model parameters follow those in Fennel et al. (2006). Nevertheless, a series of experiments is conducted to evaluate model sensitivity to the parameter range in Fennel et al. (2006). The experimental results show that the adjustment of parameters, e.g., the growth rate of phytoplankton or the maximal zooplankton grazing rate, can integrally change the content of the primary production, whereas the distribution patterns of primary production are not changed markedly in the strait. However, the model results are sensitive to the sinking velocities of detritus (Wang et al., 2013), as mentioned by Fasham et al. (1990). In this study, the sinking velocities of SDET and LDET are set to 1.0 and 3.0 m day^{-1}, respectively, which are larger than those (0.1 and 1 m day^{-1}) used in Fennel et al. (2006). Model equations and parameter settings can be found in Appendices A and B, respectively.

2.3. Modeling configuration

The model is forced by 6-hourly data from the National Centers for Environmental Prediction reanalysis product (http://www.opc.ncep.noaa.gov), including wind, net shortwave and longwave radiations, and precipitation rate, etc. The open boundary conditions are derived from My Ocean Project (http://www.myocean.eu/) data. Fig. 4 shows the temporal variation of the spatially averaged wind in the TWS from 25 February to 4 March, 1998, covering the observation period. The model spin-up time is 4 years and is forced by climatological boundary conditions until reaching a stable state (Wang et al., 2013). Then, the model is forced using the 6-hourly forcing condition beginning 1 January, 1998.

2.4. Model evaluation

The model results are compared with the observed data in Fig. 5 to evaluate the model's capability to reproduce the winter bloom. The in-situ measurements were obtained during a relaxation of the north-easterly wind on 2–3 March, 1998 (indicated by the blue box in Fig. 4).

The comparison shows that the model (Fig. 5b, d and f) captures the basic water mass distribution patterns compared to observations (Fig. 5a, c and e). The cold (<17 °C), fresh (salinity < 34 psu) and high nutrient (>4 mmol m^{-3}) MZCW flows within the western part of the section, while the relatively warmer (>19 °C), higher salinity and low-nutrient SMW occupies the middle and eastern parts of the section. The two water masses converge in the western section, and a front is formed with the dense tracer contours (temperature, salinity and nutrient), stretching from the surface of Station 9803 to the bottom layer of Station 9801 in Fig. 5. Temperature and salinity are vertically homogenous in both the model and observation of the eastern section.

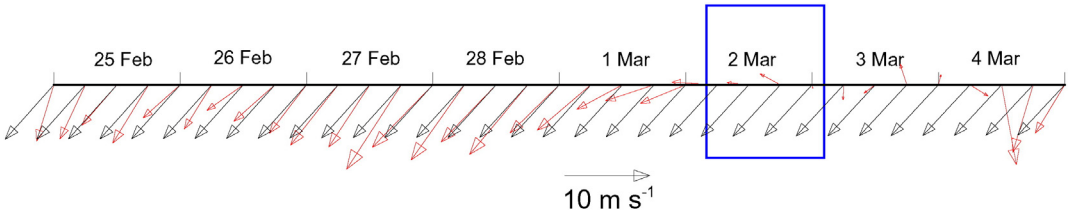

Fig. 4. Six-hourly NCEP wind (red vectors) and climatological wind (black vectors) during the period from 25 February to 4 March in 1998. The blue box indicates the observation time. (For interpretation of the references to color in this figure legend, the reader is referred to the web version of this article.)

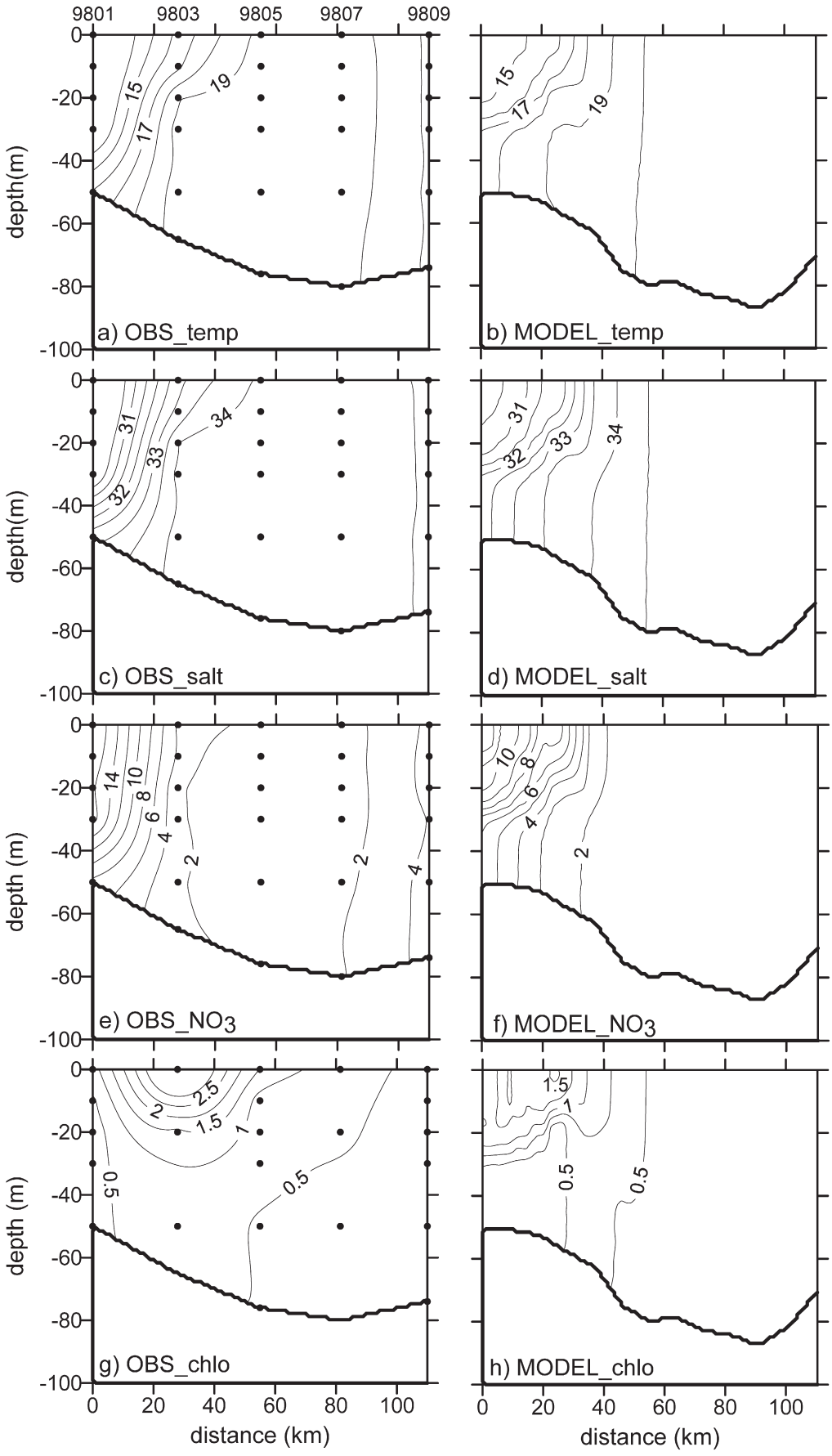

Fig. 5. Distributions of the observed (left) and modeled (right) temperature (temp; units: °C), salinity (salt; units: psu), chlorophyll-*a* (chlo; units: mg m^{-3}), and NO_3 (units: mmol m^{-3}) along the observation section (red dots in Fig. 1) on 2 March 1998.

The modeled MZCW is weaker compared to the observations, which is reflected in the thinner freshwater column at Station 9801 in the model. The deviation between the simulation and observation could be caused by an inaccuracy in the surface forcing data, boundary conditions, or the resolution of observations.

The model reproduces the observed maximal concentration of chlorophyll at Station 9803 (Fig. 5g and h), though the model underestimates the peak value. The chlorophyll maximum appears at the surface of Station 9803 and decreases with depth. Moreover, chlorophyll is lower (<0.5 mg m^{-3}) within the eastern and lower layer of the western sections in both the model and observation. However, the modeled chlorophyll is slightly higher than the observed values in the upper layer of Station 9801, which could be due to the simplified processes in the biological model. For example, the absence of suspended sediment in the model would overestimate the light intensity in the coastal water, which leads to overestimated chlorophyll.

However, for such a complicated system, the model captures the distributions of the MZCW and the SMW in the TWS during the observation period. The modeled chlorophyll patterns resemble those observed, especially the higher offshore chlorophyll.

3. Results

3.1. Modeled chlorophyll

The spatial–temporal variation of phytoplankton is analogous to that of chlorophyll, although the relationship between chlorophyll and phytoplankton is nonlinear. Hence, only chlorophyll is used in the analysis. The modeled surface chlorophyll is shown in Fig. 6.

The model shows that the chlorophyll concentration is low and relative steady in the strait (Fig. 6a–c) under strong northeasterly winds (wind speed of approximately 10 m s^{-1}) from 27 February to 1 March. The concentration is generally less than 1.0 mg m^{-3}, except within the coastal area, e.g., Pingtan Island. The chlorophyll concentration increases to 1.25 mg m^{-3} in the northwestern strait when the wind speed decreases to approximately 4 m s^{-1} on 2 March (observed time) (Fig. 6d). On 3 March, the mean wind speed decreases to 1 m s^{-1}, and the chlorophyll concentration further increases to 1.5 mg m^{-3} in the western strait (dashed box in Fig. 6e). Additionally, a chlorophyll band with concentration >2 mg m^{-3} develops off Pingtan Island (Fig. 6e).

Vertical distributions of the modeled chlorophyll along the observed section (Fig. 1) on 28 February and 3 March are shown in Fig. 7. The chlorophyll concentration clearly increases in the upper layer (approximately 0–10 m) of the western section on 3 March in Fig. 7b relative to 28 February (Fig. 7a). Additionally, the vertical chlorophyll gradient increases significantly in the western section on 3 March. Hence, chlorophyll tends to increase in the upper layer when the wind is relaxed.

In general, the modeled chlorophyll increases in the upper 10 m of northwestern TWS when the northeasterly wind is relaxed from 1 to 3 March. The maximal chlorophyll appears in the northwestern offshore region of the TWS on 3 March, which is in accordance with the observation.

3.2. Diagnostic result of the chlorophyll variation

The physical and biological effects on chlorophyll variation can be illustrated clearly from the model diagnostic result of the chlorophyll equation in Eq. (1). On left-hand side is the evolution of chlorophyll. The physical and biological terms are located on the right-hand side of

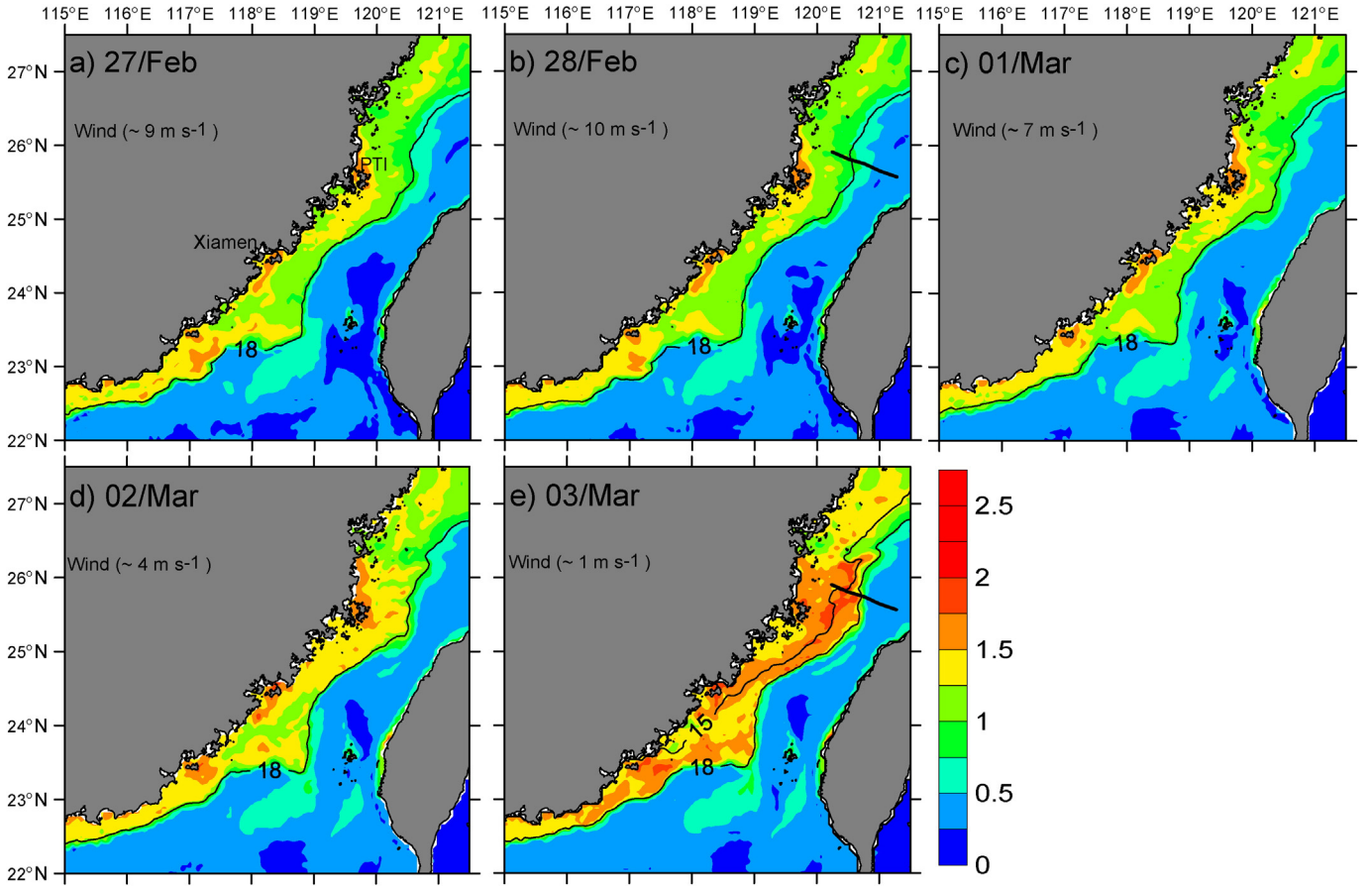

Fig. 6. Modeled sea surface chlorophyll (units: mg m^{-3}) distributions from 27 February to 3 March 1998. The black contours are 15 and 18 °C isotherms, the later one of which indicates the front location. The thick black straight line in (b) and (e) indicates the location of observation section.

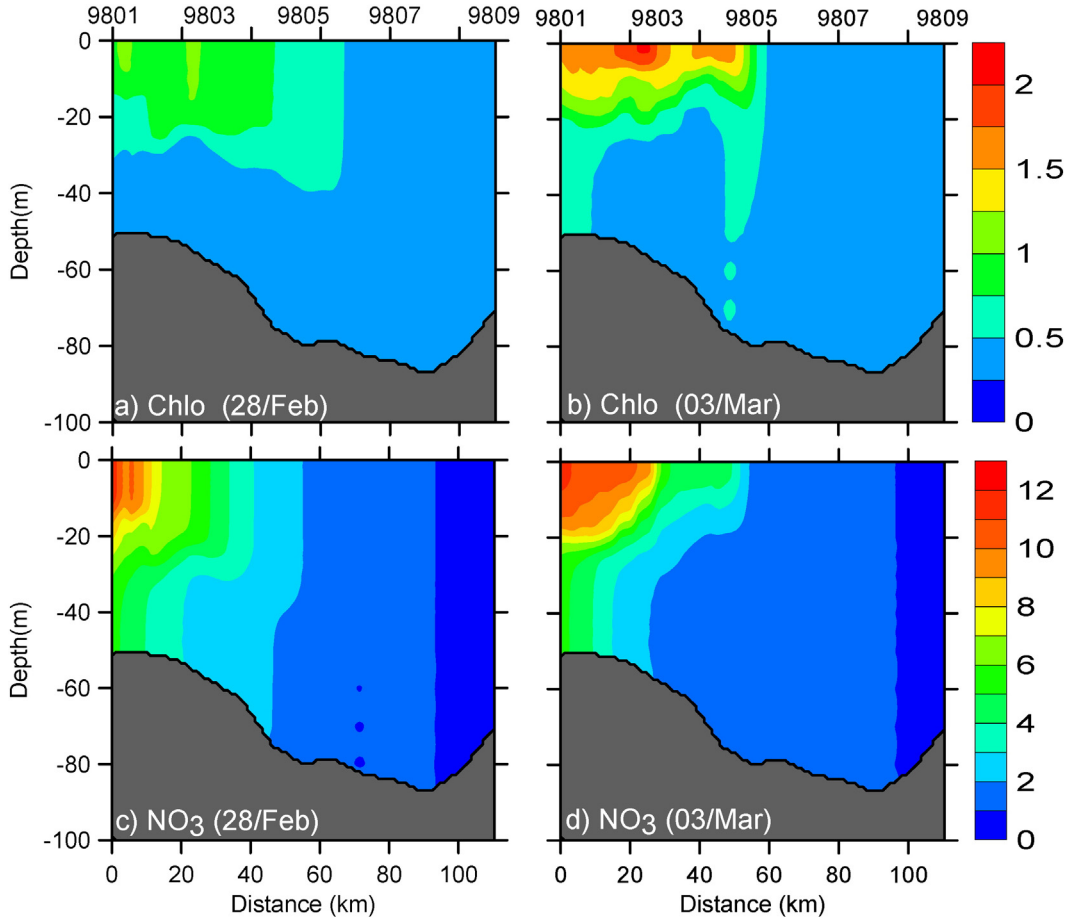

Fig. 7. Modeled distributions of chlorophyll (Chlo; units: mg m^{-3}) and NO_3 (units: mmol m^{-3}) along the observation section on 28 February (left) and 3 March (right) 1998.

the equation. The physical term includes advection, diffusion and sinking. The biological term includes phytoplankton growth and depletion, the latter of which is composed of zooplankton predation, phytoplankton mortality, and phytoplankton aggregation of small detritus.

$$\underbrace{\frac{\partial [CHLO]}{\partial z}}_{rate} = \overbrace{\underbrace{-\vec{u}\cdot\nabla[CHLO]}_{advection} + \underbrace{K_h\nabla^2[CHLO] + \frac{\partial}{\partial z}\left(K_m\frac{\partial [CHLO]}{\partial z}\right)}_{diffusion} - w\frac{\partial [CHLO]}{\partial z}}^{physical\ term}$$
$$+\overbrace{\underbrace{\mu\cdot[CHLO]}_{growth} + \underbrace{(-g\cdot[ZOOP] - m\cdot[CHLO] - \tau[CHLO])}_{depletion}}^{biological\ term} \quad (1)$$

where [*CHLO*] and [*ZOOP*] are the concentrations of chlorophyll and zooplankton, respectively. K_h and K_m are the horizontal and vertical diffusion coefficients, respectively. $\vec{u}$ is the velocity, μ is the phytoplankton growth rate, g is the zooplankton grazing rate, m is the mortality rate, τ is the rate of phytoplankton and small detritus aggregating to form large detritus, and w is the sinking velocity of phytoplankton.

The modeled chlorophyll (Figs. 6 and 7) predominately increases in the upper 10 m of the western TWS from 28 February to 3 March. Hence, the 0–10 m mean of the diagnostic terms in Fig. 8 are used, including the changing rate, advection, diffusion and the biological terms. The sinking term, which is 2 orders of magnitude smaller than the others, is negligible. The positive (red) and negative (blue) values in Fig. 8 indicate the contribution of each term to the chlorophyll increase and decrease, respectively.

On 28 February, the changing rate (Fig. 8a) of chlorophyll in the TWS is low, which is consistent with the minimally changed chlorophyll concentration from 27 to 28 February in Fig. 6. The right-hand side terms in Fig. 8b–d indicate that the low changing rate is due to the counteraction between vertical diffusion (Fig. 8c) and the biological term (Fig. 8d), while the advection (Fig. 8b) and horizontal diffusion (not shown) are negligible. In contrast, the changing rate of chlorophyll becomes positive (red color in Fig. 8e) in the western TWS on 3 March, which corresponds to the obvious increase in chlorophyll from 2 to 3 March (Fig. 6d and e). The positive changing rate in Fig. 8e is attributed to the significantly decreased diffusion term from 28 February (Fig. 8c) to 3 March (Fig. 8g). In other words, the significantly decreased diffusion from 28 February (Fig. 8c) to 3 March (Fig. 8g) leads to an increased chlorophyll concentration in the upper layer of the western TWS on 3 March (Fig. 6e). The front encompasses a large positive changing rate (Fig. 8e), primarily a result of advection, which will be explained in Section 4.3.

The vertical distributions of the diffusion and biological terms along the observed section are shown in Fig. 9 to further evaluate the increased chlorophyll as a result of decreased diffusion in Fig. 8. Fig. 9b and d indicate the two-layered structure of the biological term, which is dependent on light and nutrients. Light and nutrients are sufficient for photosynthesis in the upper layer; therefore, the phytoplankton growth rate exceeds the depletion rate, resulting in a net production of chlorophyll (positive value in Fig. 9b and d). Phytoplankton growth in the lower layer is limited by insufficient solar radiation, leading to a net decrease in chlorophyll (negative value in Fig. 9b and d). Hence, the net biological effect generates chlorophyll in the upper layer but decreases chlorophyll in the lower layer.

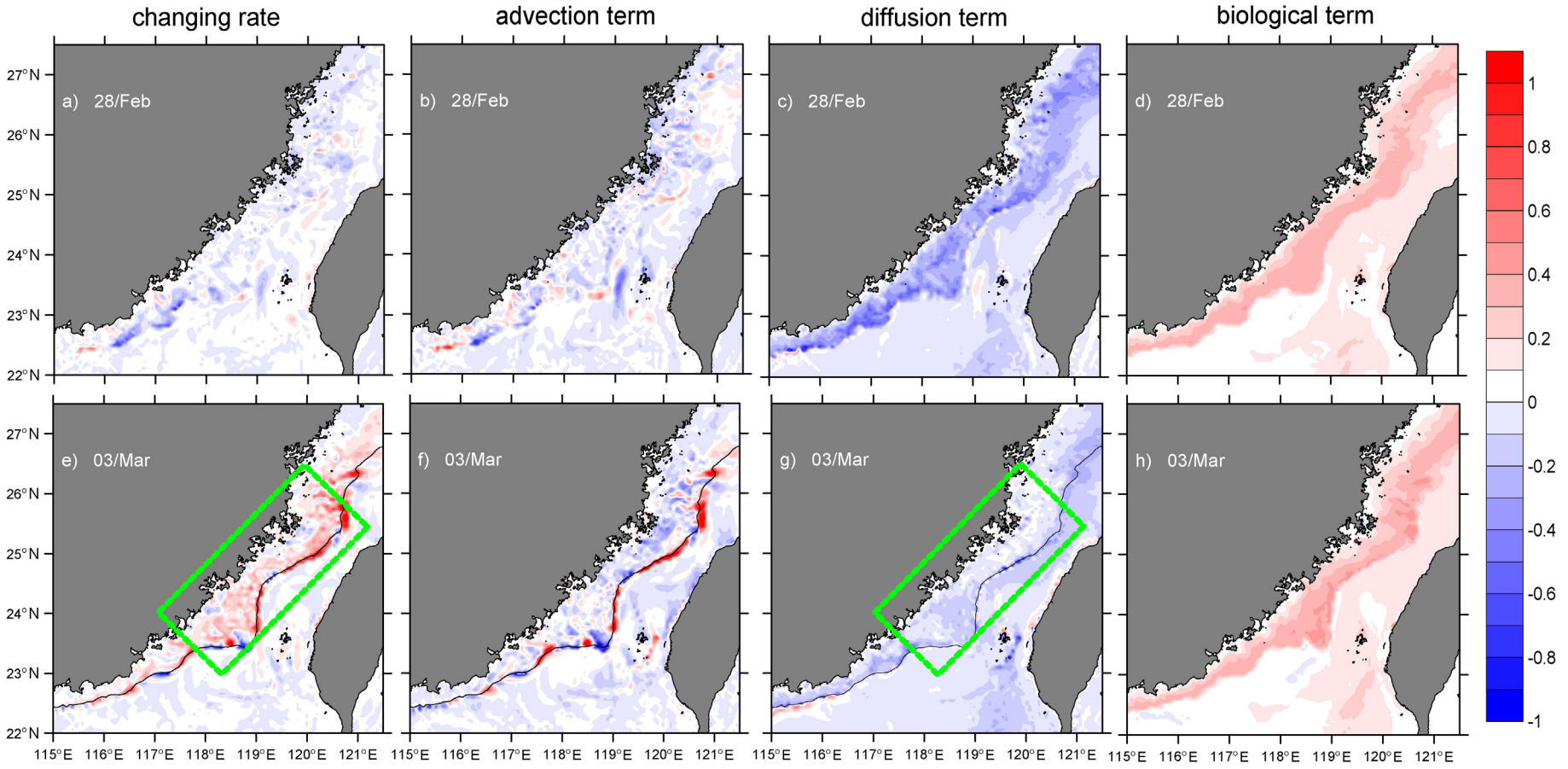

Fig. 8. Upper 10-m averaged distributions of changing rate (a, e), advection (b, f), vertical diffusion (c, g) and biological terms (d, h) in phytoplankton equation (Eq. (1)) in the TWS on 28 February (upper) and 3 March (lower) 1998. The 18 °C isotherm (black contour) in (e) and (f) indicates the approximate location of front. The green box indicates the bloom zone in the TWS (units: mg m^{-3} day^{-1}). (For interpretation of the references to color in this figure legend, the reader is referred to the web version of this article.)

Moreover, the biologically produced chlorophyll would be redistributed by vertical mixing. The diffusion term in Fig. 9a reveals an opposing pattern to the biological term (Fig. 9b) on 28 February. The negative (positive) values in the upper (lower) layers in Fig. 9a suggest that the biologically produced chlorophyll in the upper layer is transported into the lower layer through vertical mixing, leading to chlorophyll loss in the upper layer. This explains the counteraction between the diffusion (Fig. 8c) and biological (Fig. 8d) terms in the top 10 m of the western TWS on 28 February. Vertical mixing weakens when the wind relaxes from 1 to 3 March, and the loss of chlorophyll through vertical diffusion decreases in the western TWS, as indicated by the diffusion term on 3 March in Figs. 8g and 9c. The net production of chlorophyll (Figs. 8h and 9d) exceeds the diffusive loss (Figs. 8g and 9c) in the upper layer of the western TWS, leading to the chlorophyll increase in the western TWS (positive changing rate in Fig. 8e).

The diagnostic analysis indicates that the net production of chlorophyll in the upper layer is nearly balanced by the downward transport of chlorophyll through vertical mixing under the condition of strong wind (e.g., 28 February), resulting in the steady low chlorophyll concentration in the TWS. In contrast, the net production of chlorophyll in the upper layer is mixed less into the lower layer under the condition of weak wind (e.g., 3 March), which allows the phytoplankton to aggregate and rapidly reproduce in the upper layer of the western TWS.

3.3. Hydrodynamic processes

Model diagnostic results illustrate that the cause for the increased chlorophyll in the upper layer of the western TWS is weakened mixing. Hence, model hydrodynamic results are shown to verify this weakened mixing.

3.3.1. Circulation adjustment

The northeasterly wind is generally inconsistent in the TWS in winter, relaxing on a weekly to biweekly period (Chen, 1982; Lin et al., 2005). In the winter of 1998, the northeasterly wind persists from 25 to 28 February, and the maximal wind speed (approximately 10 m s^{-1}) appears stronger on 28 February than the climatological winter wind (constant black vectors in Fig. 4). Subsequently, the wind gradually relaxes from 1 to 3 March, and a minimal wind speed (<1 m s^{-1}) appears on 3 March. Fig. 10 shows the simulated surface circulations on 28 February and 3 March, corresponding to the strongest and weakest winds, respectively.

On 28 February (Fig. 10a), the strong northeasterly wind forces the cold, fresh MZCW to flow southward along the west coast of the TWS, while the warm SMW northward intrudes from the Penghu Channel. Due to the shallow topography of the Zhangyun Ridge, an anticyclonic current is formed to maintain potential vorticity conservation. This result is similar to the general winter TWS circulation structure proposed by Jan et al. (2002). The current flows uniformly northward and the SMW increases (Fig. 10b) when the wind relaxes on 3 March. Additionally, the current appears offshore of Pingtan Island, which is consistent with the studies by Liao et al. (2013); Oey et al. (2014), and Lin et al. (2005). Those studies found that the MZCW would turn offshore when the wind was relaxed. The cause for offshore flow was explained by Liao et al. (2013) as a geostrophic adjustment. When the northeasterly wind relaxed, the northward pressure gradient southeast

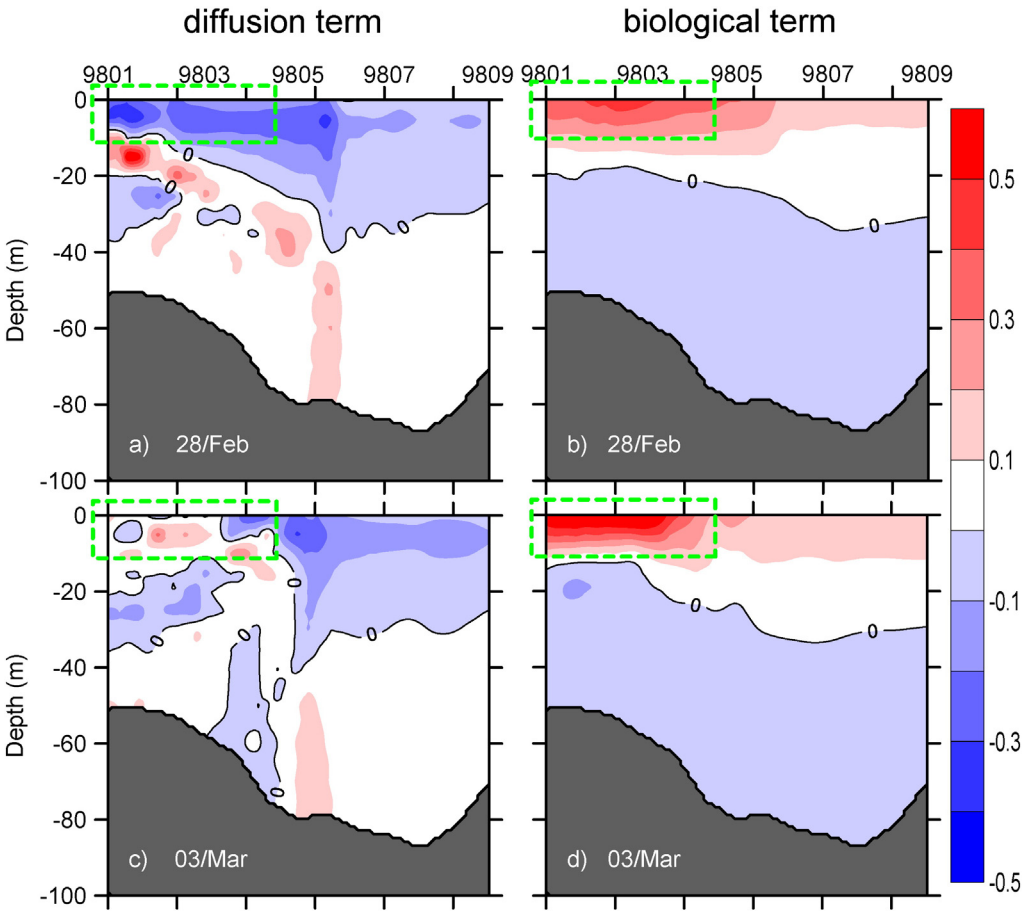

Fig. 9. Vertical distributions of the diffusion (a, c) and biological terms (b, d) in the phytoplankton equation (Eq. (1)) along the observation section on 28 February (upper) and 3 March (lower) 1998. The solid line is zero contour and the green box indicates the bloom zone in the section. (units: mg m^{-3} day^{-1}). (For interpretation of the references to color in this figure legend, the reader is referred to the web version of this article.)

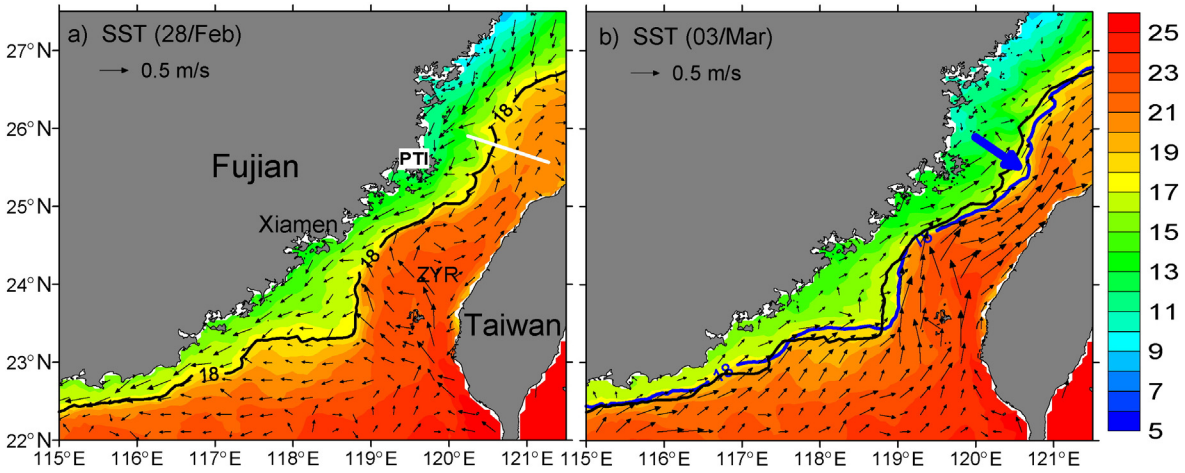

Fig. 10. Simulated surface circulation (units: m s^{-1}) with the background showing sea surface temperature (SST; units: °C) on 28 February (a) and 3 March (b) 1998. The black and blue contours are 18 °C isotherm on 28 February and 3 March, respectively. The offshore shift of the 18 °C isotherm off Pingtan Island (PTI) in (b) indicates the presence of cross-strait flow. The white line in (a) is the section linking stations "9801" and "9809" in Fig. 1. (For interpretation of the references to color in this figure legend, the reader is referred to the web version of this article.)

of Pingtan Island would generate the offshore component of geostrophic current. Oey et al. (2014) labeled the offshore current a cross-strait flow, which was explained by the amplification of a finite-amplitude meander downstream of the Zhangyun Ridge, where a strong cyclone developed.

3.3.2. Stratification and weakened mixing

The cross-strait flow causes the offshore movement of the cold MZCW in the northwestern TWS, which is indicated by a shift in the 18 °C isotherm off Pingtan Island in Fig. 10b. The offshore fresh MZCW would flow above the dense SMW via the buoyancy effect, which intensifies the stratification between two water masses.

The vertical distributions of temperature and salinity along the observed section (white line in Fig. 10a) on 28 February and 3 March are shown in Fig. 11. The basic features include the occupation of the dense SMW in the eastern part of the section, with vertically homogeneous distributions of temperature and salinity from Stations 9805 to 9809 (Fig. 11a–d). In contrast, the fresh MZCW is located weakly within the upper layer of the western section from Stations 9801 to 9803.

On 28 February, the cold (<18 °C) and fresh (<33 psu) MZCW is more onshore and deeply occupies the western TWS, forced by the Ekman effect under strong northeasterly winds. The temperature and salinity are vertically homogenous in the upper 20 m from Stations 9801 to 9803, and the front stretches from a depth of 20 m at Station 9801 to 40 m at Station 9805. The stratification between the MZCW and SMW is weak, with small temperature and salinity gradients (Fig. 11a and c). In contrast, the cold and fresh MZCW extends more offshore and thins while flowing over the SMW on 3 March (Fig. 11b and d). The front location is lifted, and the stratification is greatly intensified in the upper layer between Stations 9803 and 9805 with increased temperature and salinity gradients.

Mixing in the TWS is weakened due to the intensified stratification and reduced surface turbulence input. The stratification intensity and mixing can be quantified using the Brunt–Vaisala frequency and diffusion coefficient, respectively (Fig. 11). The stratification intensity increases by 1 order of magnitude from 28 February to 3 March, where the Brunt–Vaisala frequency changes from approximately $10^{-3.5}$–10^{-3} to 10^{-2} s^{-1} in the upper 20 m between the Stations 9803 and 9805 (Fig. 11e and f). Mixing decreases by 2 orders of magnitude as the diffusion coefficient changes from $10^{-2.5}$–10^{-2} to 10^{-5}–10^{-4} m^2 s^{-1} (Fig. 11g and h). Moreover, the position of the weakened mixing is coincident with increased chlorophyll, which supports the diagnostic analysis.

4. Discussion

4.1. Mixing effect on phytoplankton bloom

Strong mixing can rapidly transport phytoplankton from the upper layer into the lower layer, restraining the phytoplankton from increasing in the upper layer. Wherein the loss of phytoplankton through diffusion can be complemented by production in the upper layer under a weak mixing condition, the phytoplankton will increase, leading to bloom. This regulation on the phytoplankton bloom is also clearly illustrated in our model diagnostic result in Section 3.2.

An analytical critical turbulence model based on phytoplankton regulation was proposed by Taylor and Ferrari (2011) to quantitatively estimate the mixing effect on bloom initiation. An equation that balances the net production and mixing-induced loss of phytoplankton in the upper layer is developed, and thus a critical turbulence coefficient K_{cr} is derived in Eq. (2) (Taylor and Ferrari, 2011). The bloom occurs under the condition that the vertical mixing is less than

$$K_{cr} = \mathrm{h}^2 \frac{(\mu - m)^2}{m}, \tag{2}$$

where K_{cr} is the critical turbulence coefficient, h is the depth of the upper layer (10 m in this study), m is the mortality rate of phytoplankton, and μ is the local growth rate of phytoplankton.

First, the applicability of the critical turbulence model is satisfied. The basic assumption in the model is that there are sufficient nutrients for phytoplankton growth. The MZCW in our case carries abundant nutrients into the TWS in winter, and the nutrient concentration is high (2–15 mmol m^{-3}) in the western strait (Fig. 7c and d). Observations also suggest that the nutrients are not the limiting factor for phytoplankton growth in the western TWS in winter (Naik and Chen, 2008; Zhang and Huang, 2000). Hence, our analysis is limited in the western part (0–50 km) of the section where nutrient concentration is sufficient.

Next, we take the depth of upper layer (h) equal to 10 m in the critical turbulence model, according to the increased chlorophyll concentration in Fig. 7b. The vertically averaged diffusion coefficient in the top 10 m is plotted as the dashed line, and the derived critical turbulence coefficient is plotted as the solid line in Fig. 12. The average K_{cr} along the western section is approximately $10^{-1.8}$ and $10^{-1.9}$ m^2 s^{-1} on 28 February and 3 March, respectively. The slight difference between the K_{cr} on 28 February and 3 March is primarily caused by the change in μ_0 related to chlorophyll-induced light attenuation. The critical

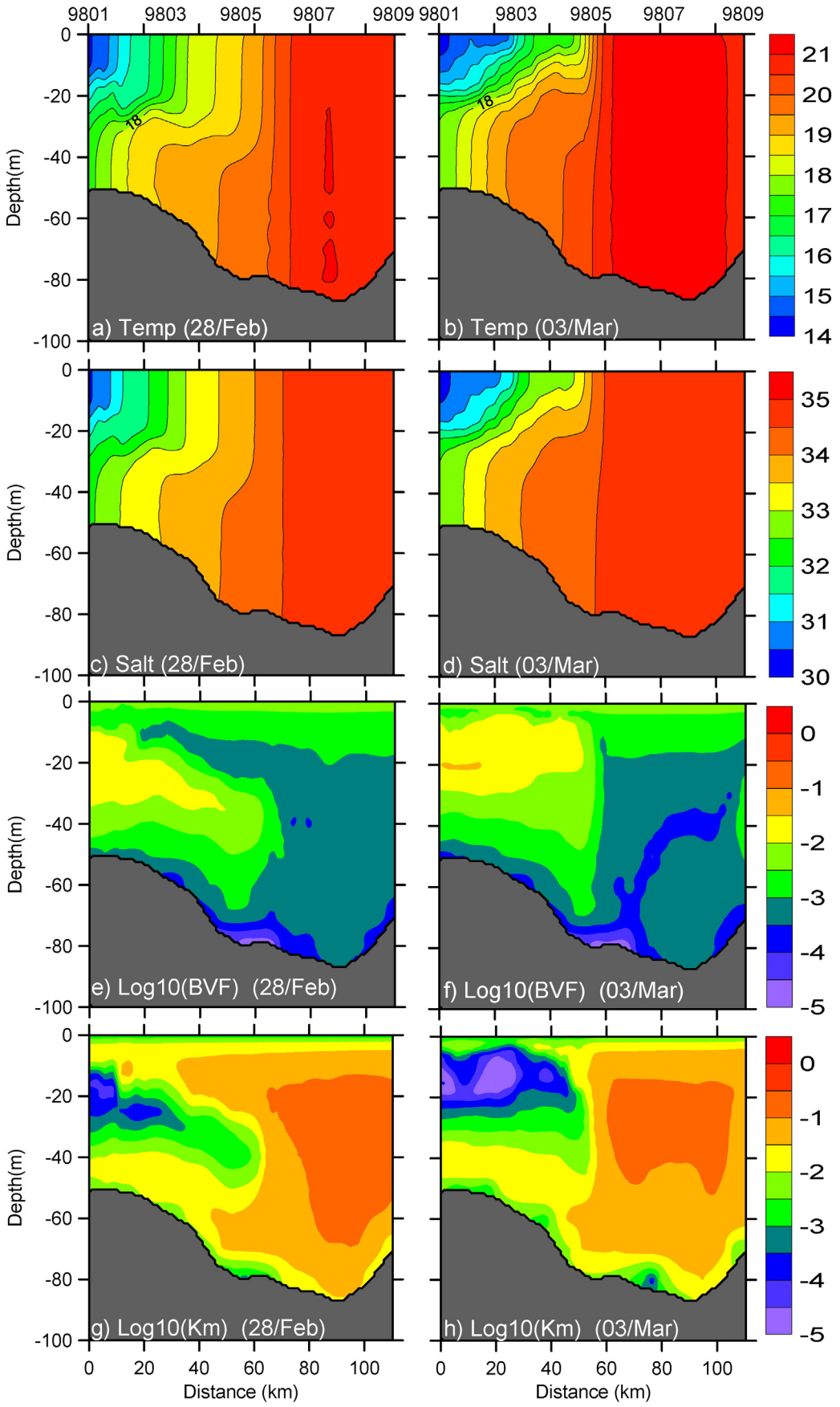

Fig. 11. Distributions of modeled temperature (units: °C) (a and b) and salinity (units: psu) (c and d) and logarithm (10 base) of Brunt–Vaisala frequency (BVF, units: s^{-1}) (e and f) and vertical diffusion coefficient (K_m, units: $m^2\ s^{-1}$) (g and h) along the observation section (red dots in Fig. 1) on 28 February (left) and 3 March (right) 1998.

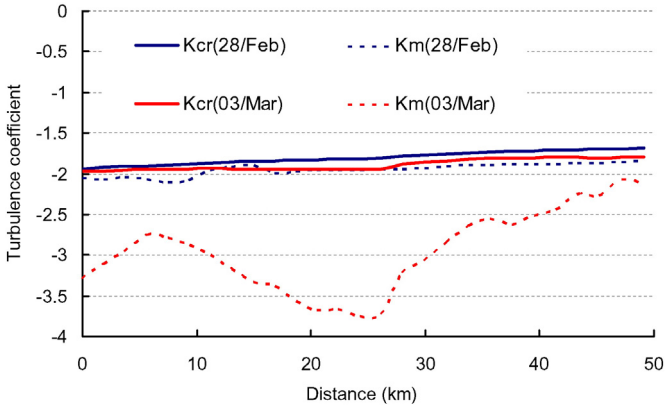

Fig. 12. Logarithm of critical turbulence coefficient (Kcr; units: $m^2\ s^{-1}$) in the critical turbulence model and vertical diffusion coefficient (K_m; units: $m^2\ s^{-1}$) in the model along the western part of the section on 28 February (blue) and 3 March (red) 1998. Solid lines are the critical turbulence coefficient, and dashed lines are the vertical diffusion coefficient in the model. (For interpretation of the references to color in this figure legend, the reader is referred to the web version of this article.)

turbulence coefficient (K_{cr}) for the bloom in the TWS in winter is estimated to be approximately $10^{-2}\ m^2\ s^{-1}$. On 28 February, the average diffusion coefficient (blue dashed line) is approximately $10^{-1.9}\ m^2\ s^{-1}$, which is similar to the estimated K_{cr} (blue solid line). This result suggests that chlorophyll is relatively steady in the upper layer of the western section due to the balance between the production and mixing-induced loss of phytoplankton. As the wind relaxes on 3 March, the averaged diffusion coefficient (red dashed line) in the upper layer is one order of magnitude smaller than the K_{cr} (red solid line), which suggests that production is greater than the mixing-induced loss of phytoplankton. Phytoplankton that increases in the upper layer leads to bloom production.

The critical turbulence model result confirms the coupled model result, where increased chlorophyll in the western TWS is caused by weakened vertical mixing. Additionally, the critical turbulence intensity that controls bloom occurrence is approximately $10^{-2}\ m^2\ s^{-1}$ in the TWS in winter.

4.2. Stratification effect on reduced mixing

The model result has demonstrated that the cause for the winter bloom in the TWS is weakened vertical mixing. Weakened mixing could be generated by both reduced surface turbulence input and intensified stratification. Their contributions are distinguished according to the following two facts.

First, the diffusion coefficients in Fig. 11g and h change greatly in the western section but change little in the eastern under the same turbulence input condition on 3 March. However, the coefficient change matches the stratification (Brunt–Vaisala frequency in Fig. 11f) in the western section. This result suggests that the reduced direct turbulence input has a lesser effect on the weakened mixing in the TWS during the wind relaxation. In contrast, the intensified stratification plays more dominant role.

Secondly, a numerical sensitivity experiment is completed by neglecting the buoyancy (vertical density gradient) effect in the MY-2.5 turbulence closure model (Mellor and Yamada, 1982) on 3 March. The results (Fig. 13) indicate that the vertical diffusion coefficient (Fig. 13a) in the western strait is obviously larger than that in Fig. 11h, and the chlorophyll concentration (Fig. 13b) is reduced due to the strong mixing. The experimental results further confirm that the dominant role in the weakened mixing in the western TWS is a result of intensified stratification rather than the reduced surface turbulence input. Moreover, relaxed wind acts as a trigger, which extends the diluted MZCW offshore, intensifies stratification and weakens mixing.

4.3. Chlorophyll offshore advection

A significant positive advection effect is apparent at the frontal zone, as mentioned in Section 3.2 (Fig. 8f). Hence, the advective transport of chlorophyll might also contribute to offshore bloom when the wind is relaxed.

The maximal advection term on 2 March is plotted in Fig. 14a with red shadows; the frontal movement between 2 and 3 March is indicated by the 18 °C isotherms. Because the front encompasses the largest horizontal chlorophyll gradient (as shown in Fig. 6), the advection effect is a maximum at the transition zone between the fronts on 2 and 3 March, which indicates that the high chlorophyll concentration in the western TWS is transported eastward by the cross-strait flow. The shadows indicating the maximal chlorophyll concentration on 1–3 March are superimposed in Fig. 14b to clearly show the formation of the offshore maximal chlorophyll with time. The maximal chlorophyll band is closer to the shore on 1 March (green shadow in Fig. 14b). Subsequently, the near-shore high chlorophyll concentration (green shadow) is located offshore and transported downstream by the circulation, forming a continuous offshore band with maximal chlorophyll on 3 March (red shadow in Fig. 14b). Simultaneously, the concentration of the maximal chlorophyll band increases due to weakened mixing.

The biological, advection and diffusion terms in Eq. (1) are averaged in the western TWS to quantitatively evaluate the roles of weakened mixing and offshore advection on bloom production. The region west of the 18 °C isotherm indicates the western TWS, and the area between

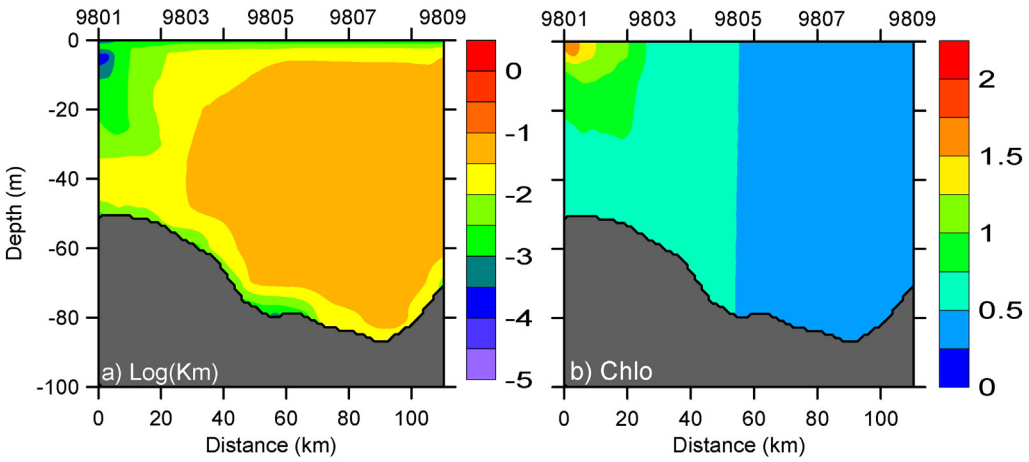

Fig. 13. Distributions of logarithm of vertical diffusion coefficient (units: $m^2\ s^{-1}$; left panel) and chlorophyll (Chlo) (units: $mg\ m^{-3}$; right panel) along the observation section on 3 March 1998 in the sensitive experiment, which has neglected the buoyancy (vertical density gradient) effect in the MY-2.5 turbulence calculation.

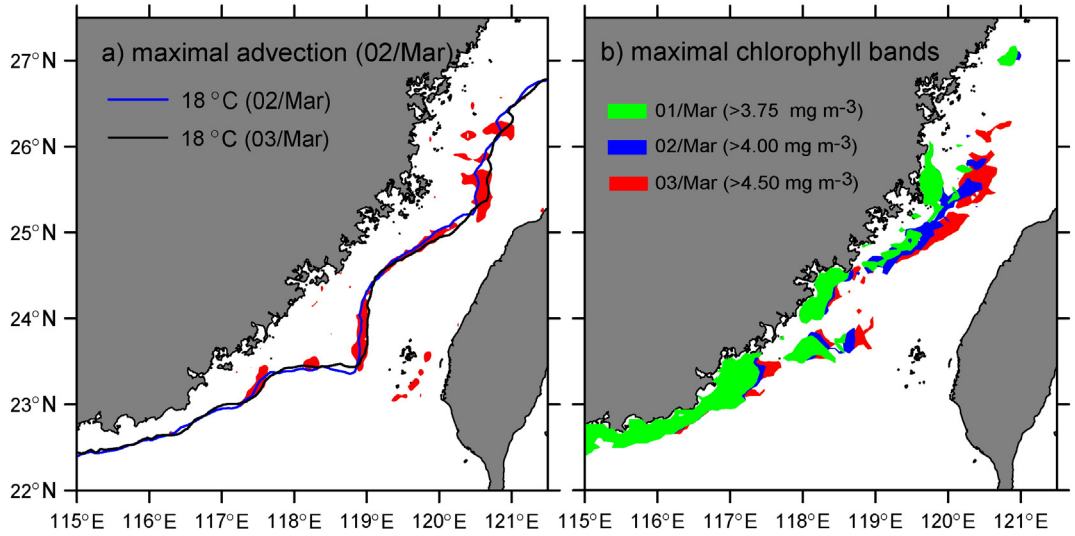

Fig. 14. (a) Maximal advection terms (>0.3 mg m^{-3}) on 2 March (blue and black contours are 18 °C isotherm on 2 and 3 March, respectively). (b) Bands of maximal chlorophyll concentration on 1, 2 and 3 March, 1998. (For interpretation of the references to color in this figure legend, the reader is referred to the web version of this article.)

the 15 and 18 °C isotherms indicates the frontal region. The roles of weakened mixing and offshore advection on bloom production are evaluated by their contributions to the increasing rate of chlorophyll from 1 to 3 March.

The results show that the weakened diffusion term plays a dominant role (approximately 70%) in the increased chlorophyll concentration in the western TWS from 28 February to 3 March, while the advection term contributes 30%. The contribution of advection increases to 37% and that of weakened mixing decreases to 56% in the frontal region, illustrating the increased role of the advection term.

5. Summary

An offshore phytoplankton bloom occurs occasionally in the north-central TWS in winter, and the mechanisms have not been reported prior this study. The coupled physical–biological model results indicate that the relaxation of a northeasterly wind is the trigger for bloom production. The stratification and advection associated with the MZCW offshore extension under relaxed wind are two controlling factors in the occurrence of offshore bloom. The quantitative contribution of weakened mixing on the bloom is 70% and that of advection is 30% on average. The model study helps to explain the mechanisms behind the exceptional winter bloom formation in the TWS.

Acknowledgments

We are grateful F. Zhang from Fujian Institute of Oceanography provided the observed data. We thank two anonymous reviewers for their constructive comments and suggestions that helped to improve the manuscript. This work is supported by grant (2013CB955704) from the National Basic Research Program of China; grant (41476005) from the Natural Science Foundation of China (NSFC); grant (U1305231) from NSFC and Fujian Province; National Key Technology R&D Program (2013BAB04B00); and grant (2014M551838) from China Post-doctoral Foundation Funding Project.

Appendix A. Biological model equations

The general equation for the biological variable C is

$$\frac{\partial [C]}{\partial t} = -\vec{v}\cdot\nabla[C] + K_h\nabla^2[C] + \frac{\partial}{\partial z}\left(K_m\frac{\partial [C]}{\partial z}\right) + B_C \tag{A1}$$

where $[C]$ is the concentration of C, C include PHYTO, CHLO, ZOOP, NO_3, NH_4, SDET, and LDET, as defined in Section. 2.2. $\vec{v}$ is the three-dimensional velocity, and K_h and K_m are the horizontal and vertical diffusion coefficients, respectively. The biological process related changing rate is marked by B_C, which is calculated in the biological model. B_C of each biological variables is introduced as follows and the schematic for them can be seen in Fig. 2. More descriptions are detailed in Fennel et al. (2006).

$$B_{\mathrm{PHYTO}} = t_{PP\max}\cdot\left(L_{\mathrm{NO_3}}+L_{\mathrm{NH_4}}\right)\cdot[\mathrm{PHYTO}] - t_{Pmort}\cdot[\mathrm{PHYTO}] - L_{coag}\cdot[\mathrm{PHYTO}] - L_{graze}\cdot[\mathrm{ZOOP}] - w_P\frac{\partial[\mathrm{PHYTO}]}{\partial z} \tag{A2}$$

$$B_{\mathrm{CHLO}} = \rho_{\mathrm{CHLO}}\cdot t_{PP\max}\cdot\left(L_{\mathrm{NO_3}}+L_{\mathrm{NH_4}}\right)\cdot[\mathrm{CHLO}] - t_{Pmort}\cdot[\mathrm{CHLO}] - L_{coag}\cdot[\mathrm{CHLO}] - L_{graze}\cdot[\mathrm{ZOOP}]\cdot\frac{[\mathrm{CHLO}]}{[\mathrm{PHYTO}]} - w_P\frac{\partial[\mathrm{CHLO}]}{\partial z} \tag{A3}$$

$$B_{\mathrm{ZOOP}} = \beta\cdot L_{graze}\cdot[\mathrm{ZOOP}] - t_{Zmeta}\cdot[\mathrm{ZOOP}] - t_{Zmort}\cdot[\mathrm{ZOOP}]^2 - t_{Zexc}\cdot L_{graze}\cdot\beta\cdot[\mathrm{ZOOP}]/g_{\max} \tag{A4}$$

$$B_{\mathrm{SDET}} = (1-\beta)\cdot L_{graze}\cdot[\mathrm{ZOOP}] + t_{Pmort}\cdot[\mathrm{PHYTO}] + t_{Zmort}\cdot[\mathrm{ZOOP}] - L_{coag}\cdot[\mathrm{SDET}] - t_{SDre}\cdot[\mathrm{SDET}] - w_{SD}\frac{\partial[\mathrm{SDET}]}{\partial z} \tag{A5}$$

$$B_{\mathrm{LDET}} = L_{coag}\cdot([\mathrm{SDET}]+[\mathrm{PHYTO}]) - t_{LDre}\cdot[\mathrm{LDET}] - w_{LD}\frac{\partial[\mathrm{LDET}]}{\partial z} \tag{A6}$$

$$B_{\mathrm{NO_3}} = -t_{PP\max}\cdot L_{\mathrm{NO_3}}\cdot[\mathrm{PHYTO}] + L_{nitri}\cdot[\mathrm{NH_4}] \tag{A7}$$

$$B_{\mathrm{NH_4}} = -t_{PP\max}\cdot L_{\mathrm{NH_4}}\cdot[\mathrm{PHYTO}] - L_{nitri}\cdot[\mathrm{NH_4}] + (t_{Zmeta}+t_{Zexc})\cdot[\mathrm{ZOOP}] + t_{SDre}\cdot[\mathrm{SDET}] + t_{LDre}\cdot[\mathrm{LDET}]. \tag{A8}$$

Some parameters in Eqs. (A2)–(A8) are described as following and the others are shown in Appendix B.

$$t_{PP\max} = V_p(T)\cdot f(I);$$

$$V_p(T) = \mu_0\cdot 1.066^T;$$

$$f(I) = \frac{\alpha\cdot I}{\sqrt{V_p^2+\alpha^2\cdot I^2}};$$

$$I(z) = I_0 \cdot par \cdot e^{\left(K_w \cdot z - K_{Chlo} \int_z^0 [CHLO]\,dz'\right)},$$

where $t_{PP\max}$ is the temperature (T) and light (I) dependent rate of phytoplankton growth.

$$L_{NO_3} = \frac{[NO_3]/K_{NO_3}}{1 + [NO_3]/K_{NO_3}} \cdot I_{NH_4};$$

$$L_{NH_4} = \frac{[NH_4]/K_{NH_4}}{1 + [NH_4]/K_{NH_4}};$$

$$I_{NH_4} = \frac{1}{1 + [NH_4]/K_{NH_4}},$$

where L_{NO_3} and L_{NH_4} are nutrient limitation to phytoplankton growth by NO_3 and NH_4, respectively. The existent of NH_4 can limited NO_3 absorption by phytoplankton by factor I_{NH_4}.

$$L_{coag} = t_{coag} \cdot ([SDET] + [PHYTO]),$$

$$L_{graze} = g_{\max} \cdot \frac{[PHYTO]^2}{K_{Phyto} + [PHYTO]^2},$$

$$\rho_{CHLO} = \frac{\theta_m \cdot t_{PP\max} \cdot (L_{NO_3} + L_{NH_4}) \cdot [PHYTO]}{\alpha \cdot I \cdot [CHLO]},$$

$$L_{nitri} = n_{\max} \cdot \left(1 - \max\left[0, \frac{I - I_{thNH4}}{k_I + I - \cdot I_{thNH4}}\right]\right),$$

where L_{coag} is the aggregation rate of small detritus and phytoplankton, L_{graze} is the rate of phytoplankton grazing by zooplankton, ρ_{CHLO} is the fraction between phytoplankton and chlorophyll biomass, L_{nitri} is the nitrification rate between NH_4 and NO_3.

Appendix B. Biological parameters in Appendix A

Table B1
Biological model parameters.

Parameters	Means	Units	Values
μ_0	Phytoplankton growth rate at 0 °C	d^{-1}	0.69
K_{NO_3}	Half-saturation concentration for NO_3 absorption by phytoplankton	mmol m^{-3}	0.5
K_{NH_4}	Half-saturation concentration for NH_4 absorption by phytoplankton	mmol m^{-3}	0.5
α	Initial slope of P–I curve	mol C g $Chlo^{-1}$ $(W\ m^{-2})^{-1}\ d^{-1}$	0.125
t_{Pmort}	Phytoplankton mortality rate	d^{-1}	0.15
t_{coag}	Aggregation parameter	$(mmol\ m^{-3})^{-1}$ d^{-1}	0.005
$g_{\max}$	Maximum grazing rate of zooplankton	$(mmol\ m^{-3})^{-1}$ d^{-1}	0.6
par	Fraction of light for photosynthesis	–	0.43
K_w	Light attenuation coefficient for water	m^{-1}	0.04
K_{CHLO}	Light attenuation coefficient for chlorophyll	mg $Chlo^{-1}$ m^{-2}	0.025
K_{Phyto}	Half-saturation concentration of phytoplankton ingestion by zooplankton	$(mmol\ m^{-3})^2$	2
θ_m	Maximum ratio of chlorophyll to phytoplankton	mg Chlo mg C^{-1}	0.025
$n_{\max}$	Maximum nitrification rate	d^{-1}	0.05
K_I	Light intensity at which the inhibition of nitrification is half-saturated	W m^{-2}	0.1
I_{thNH4}	Threshold for light-inhibition of nitrification	W m^{-2}	0.0095
β	Assimilation efficiency of zooplankton	–	0.75
t_{Zmeta}	Excretion rate of basal metabolism	d^{-1}	0.1
t_{Zmort}	Zooplankton mortality rate	$(mmol\ m^{-3})^{-1}$ d^{-1}	0.025
t_{Zexc}	Maximum rate of zooplankton assimilation accompanying excretion	d^{-1}	0.1
t_{SDre}	Remineralization rate of small detritus	d^{-1}	0.03
t_{LDre}	Remineralization rate of large detritus	d^{-1}	0.01
w_P	Sinking velocity of phytoplankton	m d^{-1}	0.1
w_{SD}	Sinking velocity of small detritus	m d^{-1}	1.0
w_{LD}	Sinking velocity of large detritus	m d^{-1}	3.0

References

Chen, C.S., 1982. A preliminary study on the response of Taiwan Strait to winter monsoon. Acta Oceanogr. Taiwan. 13, 124–139.

Eppley, R.W., 1972. Temperature and phytoplankton growth in the sea. Fish. Bull. 70, 1063–1085.

Evans, G.T., Parslow, J.S., 1985. A model of annual plankton cycles. Biol. Oceanogr. 3, 327–347.

Fasham, M.J.R., Ducklow, H.W., McKelvie, S.M., 1990. A nitrogen-based model of plankton dynamics in the oceanic mixed layer. J. Mar. Res. 48, 591–639.

Fennel, K., Wilkin, J., Levin, J., Moisan, J., O'Reilly, J., Haidvogel, D., 2006. Nitrogen cycling in the Middle Atlantic Bight: result from a three-dimensional model. Glob. Biogeochem. Cycles.

Geider, R.J., McIntyre, H.L., Kana, T.M., 1996. A dynamic model of photoadaptation in phytoplankton. Limnol. Oceanogr. 41, 1–15.

Geider, R.J., McIntyre, H.L., Kana, T.M., 1997. Dynamic model of phytoplankton growth and acclimation: responses of the balanced growth rate and the chlorophyll a: carbon ratio to light, nutrient-limitation and temperature. Mar. Ecol. Prog. Ser. 148, 187–200.

Hu, J.Y., Kawamura, H., Li, C.Y., Hong, H.S., Jiang, Y.W., 2010. Review on current and seawater volume transport through the Taiwan Strait. J. Oceanogr. 66, 591–610.

Jan, S., Wang, J., Chern, C.S., Chao, S.Y., 2002. Seasonal variation of the circulation in the Taiwan Strait. J. Mar. Syst. 35, 249–268.

Liao, E.H., Jiang, Y.W., Li, L., Hong, H., Yan, X.H., 2013. The cause of the 2008 cold disaster in the Taiwan Strait. Ocean Model. 62, 1–10.

Lin, S.F., Tang, T.Y., Jan, S., Chen, C.J., 2005. Taiwan strait current in winter. Cont. Shelf Res. 25, 1023–1042.

Mellor, G.L., 2001. One-dimensional, ocean surface modeling, a problem and a solution. J. Phys. Oceanogr. 31, 790–809.

Mellor, G.L., Yamada, T., 1982. Development of a turbulence closure model for geophysical fluid problems. Rev. Geophys. Space Phys. 20, 851–875.

Naik, H., Chen, C.C.A., 2008. Biogeochemical cycling in the Taiwan Strait. Estuar. Coast. Shelf Sci. 78, 603–612.

Oey, L.-Y., Chang, Y.-L., Lin, Y.-C., Chang, M.-C., Varlamov, S., Miyazawa, Y., 2014. Cross flows in the Taiwan Strait in winter. J. Phys. Oceanogr. 44, 801–817.

Shchepetkin, A.F., McWilliams, J.C., 2005. The regional oceanic modeling system (ROMS): a split-explicit, free-surface, topography-following-coordinate oceanic model. Ocean Model. 9, 347–404.

Soetaert, K., Middelburg, J.J., Herman, P.M.J., Buis, K., 2000. On the coupling of benthic and pelagic biogeochemical models. Earth Sci. Rev. 51, 173–201.

Song, Y.H., Haidvogel, D., 1994. A semi-implicit ocean circulation model using a generalized topography-following coordinate system. J. Comput. Phys. 115, 228–244.

Taylor, J.R., Ferrari, R., 2011. Shutdown of turbulent convection as a new criterion for the onset of spring phytoplankton blooms. Limnol. Oceanogr. 56, 2293–2307.

Wang, J., Chern, C.S., 1988. On the Kuroshio branch in the Taiwan Strait during wintertime. Prog. Oceanogr. 21, 469–491.

Wang, J., Hong, H., Jiang, Y., Chai, F., Yan, X.-H., 2013. Summer nitrogenous nutrient transport and its fate in the Taiwan Strait: a coupled physical–biological modeling approach. J. Geophys. Res. 118, 4184–4200.

Zhang, F., 2001. Seasonal variation features of chlorophyll-a content in Taiwan Strait. J. Oceanogr. Taiwain Strait 20, 314–318.

Zhang, F., Huang, B.Q., 2000. Affect of hydrological characteristics for the distribution and variability of chlorophyll a in the northern part of Taiwan Strait in winter. Mar. Sci. 24, 1–3 (in Chinese).